Harnessing Viscous Flow to Simplify the Actuation of Fluidic Soft Robots

Nikolaos Vasios[1], Andrew J. Gross[1],
Scott Soifer[1], Johannes T. B. Overvelde[4,*], Katia Bertoldi[1,2,3,*]

[1]J. A. Paulson School of Engineering and Applied Sciences,
Harvard University, Cambridge, MA 02138, USA
[2]Wyss Institute for Biologically Inspired Engineering,
Harvard University, Cambridge, MA 02138, USA
[3]Kavli Institute for Bionano Science and Technology,
Harvard University, Cambridge, MA 02138, USA
[4]AMOLF, Science Park 104, 1098XG Amsterdam, The Netherlands

[*]To whom correspondence should be addressed;
E-mail: bertoldi@seas.harvard.edu or overvelde@amolf.nl

Abstract

Soft robots powered by pressurized fluid have recently enabled a variety of innovative applications in areas as diverse as space exploration, search and rescue systems, biomimetics, medical surgery and rehabilitation. Although soft robots have been demonstrated to be capable of performing a number of different tasks, they typically require independent inflation of their constituent actuators, resulting in multiple input lines connected to separate pressure supplies and a complex actuation process. To circumvent this limitation, we embed the actuation sequencing in the system by connecting fluidic actuators with narrow tubes to exploit the effects of viscous flow. We developed modeling and optimization tools to identify optimal tube characteristics and we demonstrate the inverse design of fluidic soft robots capable of achieving a variety of complex target responses when inflated with a single pressure input. Our study opens avenues towards the design of a new generation of fluidic soft robots with embedded actuation control, in which a single input line is sufficient to achieve a wide range of functionalities.

Introduction

Soft robots comprising several inflatable actuators made of compliant materials have drawn significant attention over the past few years because of their ability to produce complex and adaptive motions through nonlinear deformation.[1–11] The simplicity of their design, ease of fabrication and low cost sparked the emergence of soft robots capable of walking,[12] crawling,[13] camouflaging,[14] assisting humans in grasping[15,16] and whose response can be further enhanced by exploiting elastic instabilities.[17,18] However, to achieve a particular function, existing fluidic soft robots typically require multiple input lines, since each actuator must be inflated and deflated independently according to a specific preprogrammed sequence (Fig. 1a).

In an effort to reduce the number of input lines required for actuation, band–pass valves have been designed, which can address multiple actuators individually using a single, modulated source of pressure.[19] Another interesting avenue to reduce the number of required input signals is the direct exploitation of the highly nonlinear behavior of the system without the introduction of additional stiff elements. To this end, it has been shown that a segmented soft actuator reinforced locally with optimally oriented fibers can achieve complex configurations upon inflation with a single input source.[20] Furthermore, the non–linear properties of flexible two–dimensional metamaterials have been proven effective in reducing the complexity of the required input signal.[13,21]

Here, motivated by these opportunities for simplified actuation via non–linearities, we focus on a system comprising an array of fluidic actuators interconnected via tubes and demonstrate that viscous flow in the tubes can be harnessed to achieve a wide variety of target responses through a single input (Fig. 1b). While recent experiments with poroelastic soft actuators indicate that viscous flow is a promising candidate to simplify

the actuation of soft robots,[22] the highly non–linear response of the system prohibits the identification of simple rules to guide its design. It is therefore crucial to implement robust algorithms to efficiently identify the system parameters resulting in the desired response. To this end, we first derive a model that accurately captures the viscous flow in the tubes and then combine the model with optimization to determine through inverse design the characteristics of the tubes leading to desired responses using a single input. The excellent agreement between experiments and simulations for a wide range of prescribed target responses demonstrates the robustness of our strategy. Finally, we show that our approach enables the realization of fluidic soft robots that can perform complex tasks when powered by a single pressure input, as demonstrated through the design of a simply actuated four–legged walker.

Fluidic Bending Actuators

Although the principles proposed in this study are applicable to systems comprised of any fluidic soft actuator, to demonstrate the concept, we focus on fluidic bending actuators with an embedded network of channels and chambers.[2] All actuators have length $l = 75$ mm and a rectangular cross–section $(w_c + 4t) \times (h + 3t)$ mm^2, where $w_c = 16.5$mm is the chamber width, $h = 7.5mm$ is the chamber height and $t \in [1.5, 4]$ mm corresponds to the thickness of the top layer but also affects all other dimensions. Moreover, the actuators contain eight identical chambers connected via narrow channels and are realized using two silicone rubbers with different stiffness (Fig. 2a and Supplementary Materials).

The geometry of the embedded chambers as well as the contrasting properties of the two elastomers, cause these actuators to progressively bend upon inflation in quasi–static conditions (Fig. 2b and c). While the relationship between the bending curvature κ and the supplied volume Δv is almost linear (Fig. 2d and Movie S1), their pressure–volume

response is highly nonlinear and features a pressure plateau (Fig. 2e and Movie S1) caused by the reduction in stiffness associated with the ballooning of the top layer. Our results indicate that higher values of t lead to actuators that are simultaneously stiffer and harder to bend.

Harnessing viscous flow in the tubes

Having characterized the quasi–static response of the fluidic bending actuators, we next investigate the response of the elementary system comprising two actuators connected by a tube (Fig. 3a). To begin with, we consider two identical actuators with $t = 4$ mm, connect one of them (Actuator 1, shown in blue in Fig. 3a) to the pressure source using a tube with length $L_1 = 10$ cm and internal radius $R_1 = 0.38$ mm and then connect Actuator 2 to Actuator 1 via a tube with length $L_2 = 10$ cm and internal radius $R_2 = 0.79$ mm (Fig. 3c). Upon supplying the system with air pressurized at $p_{input} = 60$ kPa for $t_{input} = 2.5$ sec (Fig. 3c), the two actuators bend simultaneously, reach the same maximum bending curvature $\kappa_{1,max} = \kappa_{2,max} \simeq 40$ m^{-1} at $t = 2.5$ sec (Fig. 3f and Movie S2) and then deflate through the inlet (since $p_{input} = 0$ kPa for $t \geq t_{input}$, converting the inlet to an outlet for the system to reset). Note that by changing p_{input} and t_{input} we are able to control the maximum curvature of the actuators. However, since in this system the tube used to connect the two actuators does not impose significant restrictions to the fluid flow, the two actuators will always bend simultaneously.

In an effort to investigate how viscous effects in the tubes can be harnessed to tune the rate of inflation of each actuator, we replace the interconnecting tube with a narrower one, characterized by $R_2 = 0.38$ mm (keeping $L_2 = 10$ cm - Fig. 3d). The experimental results shown in Fig. 3d indicate that the actuators now bend at different rates and achieve the maximum curvature at different times (Movie S3). However, we also find that

$\kappa_{2,max}$ is significantly reduced due to energy losses associated with the viscous flow in the newly introduced interconnecting narrow tube and that $\kappa_{1,max}$ is increased because of the restriction on fluid flow imposed by such a tube.

To compensate for the energy loss we replace the second actuator in our system with a more compliant one characterized by $t = 2.97$ mm (Fig. 3e). In this case, the two actuators still bend at different rates, but reach the same maximum bending curvature $\kappa_{1,max} = \kappa_{2,max} \simeq 45$ m^{-1} (Fig. 3e and Movie S4). Therefore, our simple experiments indicate that by carefully selecting both the fluidic actuators and the tubes we can tune the bending rate as well as the maximum bending curvature of the actuators. However, the highly nonlinear response of the system prohibits the direct identification of simple rules which relate its parameters to specific desired responses. To design systems capable of achieving a target response, we first derive a model that describes their behavior and then solve the inverse problem to determine the system parameters that give rise to the target response.

Forward Modeling

Since our system comprises several fluidic bending actuators connected via narrow tubes, to predict its response we need to be able to capture the behavior of the actuators and determine the amount of fluid transferred via the tubes. To this end, we focus on the $[i]$–th tube in the system, which has length L_i (Fig. 4a), circular cross section with radius R_i (with $L_i \gg R_i$) and assume that (a) the tube is rigid and not deformed by the flow; (b) the head losses due to friction at the connections between the tube and the actuators can be captured by adjusting its length to $L_{i,eq}$[23] ; (c) the flow is incompressible and laminar;

(d) the fluid velocity has the form

$$\mathbf{u} = -\frac{2}{\pi R_i^2}\frac{d\tilde{v}_i}{dt}\left[\left(\frac{r}{R_i}\right)^2 - 1\right]\mathbf{e}_z, \tag{1}$$

where $\tilde{v}_i = \int_0^t \int_0^{R_i} \mathbf{u}\cdot\mathbf{e}_z 2\pi r dr dt$ denotes the amount of fluid exchanged through the $[i]$–th tube up to time t and $\mathbf{e}_z$ identifies the tangent vector to the tube (Supplementary Materials). Under these assumptions, integration of the Navier–Stokes equations over the volume of the tube yields

$$L_{i,eq}\frac{d^2\tilde{v}_i(t)}{dt^2} = -\frac{\pi R_i^2}{\rho}(p_i - p_{i-1}) - \frac{8\mu L_{i,eq}}{R_i^2}\frac{d\tilde{v}_i(t)}{dt}, \tag{2}$$

where p_i is the pressure inside the $[i]$–th actuator and μ is the dynamic viscosity of the fluid. Since for narrow tubes with $L_i \gg R_i$, as those considered in this study, the inertia term is negligible (Supplementary Materials), Eq. (2) can be rewritten in dimensionless form as

$$\frac{d\tilde{V}_i(t)}{dT} + \xi_i\left(P_i - P_{i-1}\right) = 0, \tag{3}$$

with

$$\xi_i = \frac{\pi G R_i^4 t_{max}}{8\mu v_0 L_{i,eq}}, \tag{4}$$

where $\tilde{V}_i = \tilde{v}_i/v_0$, $P_i = p_i/G$ and $T = t/t_{max}$ are the normalized fluid volume exchanged, pressure and time respectively (v_0, G and t_{max} denoting the volume of the smallest actuator in the system, the shear modulus of the material used to fabricate the actuators and the response time of the system, respectively). Finally, since the normalized change in volume for the $[i]$–th actuator, $\Delta V_i = \Delta v_i/v_0$, can be expressed in terms of the volumetric flows exchanged through the two tubes connected to it as

$$\Delta V_i = \tilde{V}_i - \tilde{V}_{i+1}, \tag{5}$$

Eq. (3) can be rewritten as

$$\frac{d\Delta V_i(t)}{dt} + \xi_i \left(P_i - P_{i-1}\right) - \xi_{i+1} \left(P_{i+1} - P_i\right) = 0, \tag{6}$$

where the pressure inside the $[i]$–th actuator, P_i, is a function of ΔV_i. For a system comprising N fluidic actuators interconnected via narrow tubes Eq. (6) defines a system of N coupled differential equations, which, given a pressure–volume relationship for the actuators, can be solved numerically to determine the normalized change in volume for the $[i]$–th actuator as a function of time (Supplementary Materials). Once the volume history for all actuators is known, their bending curvature is determined using the corresponding curvature–volume relationship.

To verify the validity of our model, we numerically integrate Eq. (6) using the pressure–volume and curvature–volume relations of Figs. 2d and 2e to simulate the experiments reported in Fig. 3. We find that our numerical model (solid lines) can successfully reproduce the responses observed in experiments (dashed lines) for all three systems considered in Fig. 3. The capability of the numerical model to accurately capture the response of the system in configurations involving different tubes and actuators ensures that the model can be used to identify optimal configurations.

Inverse Design

While Eq. (6) can be used to predict the temporal response of arbitrary arrays of fluidic actuators connected via narrow tubes, here we are mostly interested in the inverse problem of designing a system capable of achieving particular target responses. Specifically, we focus

on systems consisting of four fluidic bending actuators characterized by $t = 4.0$, 2.9, 2.1 and 1.5 mm connected via narrow tubes (Fig. 4b) and want the $[i]$–th actuator in the array to attain a maximum bending curvature $K_{i,max} = \kappa_{i,max}/\kappa_{ref}$ ($\kappa_{ref} = \pi/l = 41.88$ m^{-1} being the curvature of a semi-circle with arc length equal to the initial length l of the actuators) at a predefined time $T_{i,max} = t_{i,max}/t_{max}$ and then to completely deflate (Fig. 4c). Specifying a rectangular pulse for the input pressure (Fig. 4b), the parameters to be determined to achieve the target response are (a) the dimensionless tube parameters ξ_i (with $i = 1$, 2, 3, 4) which uniquely define the tube geometry; (b) the magnitude of the input pressure $P_{input} = p_{input}/G$ and (c) the pressurization time $T_{input} = t_{input}/t_{max}$. To identify a set of such parameters resulting in the desired response, we minimize

$$\mathcal{Z} = \sum_{i=1}^{4} (d_i + 0.25\,\tau_i) \tag{7}$$

where τ_i denotes the amount of time that the $[i]$–th actuator spends above a threshold curvature $K_{i,thres} = 0.05 K_{i,max}$ and is introduced to ensure that the actuators quickly deflate after approaching the target point of maximum curvature. Moreover, d_i is the "distance" in the $K-T$ space between the target and actual points of maximum curvature for the $[i]$–th bending actuator (Fig. 4d),

$$d_i = \sqrt{\Delta K_i^2 + \Delta T_i^2}, \tag{8}$$

with

$$\Delta K_i = K_{i,max} - \max_T K_i(T), \tag{9}$$

$$\Delta T_i = T_{i,max} - \operatorname*{argmax}_T K_i(T). \tag{10}$$

$K_i = \kappa_i/\kappa_{ref}$ being the normalized curvature of the [i]–th actuator. Finally, we input our model Eq. (6), the actuators' behavior (Figs. 2d and 2e) and the objective function Eq. (7) into a Python implementation of the Covariance Matrix Adaptation Evolution Strategy (CMA-ES) algorithm[24] and solve the inverse problem (i.e. determine the parameters ξ_i, P_{input} and T_{input} resulting in the target response) using a population size of 50, an initial standard deviation of 0.4 and a starting point which is randomly drawn from a standard normal distribution (Supplementary Materials).

In Fig. 5 we report results for two different target responses. First, we optimize the system so that all bending actuators achieve the same bending curvature $K_{i,max} = 1.0$ at $T_{i,max} = 0.1 + (i-1)\,0.2$ (with $i = 1$, 2, 3, 4 - Fig. 5a), targeting a bending sequence. The optimization algorithm converges to the optimal solution after 80 iterations (see Fig. 5b) and indicates that, if we choose the response time to be $t_{max} = 25$ sec, the system most closely approaches the prescribed target when the tubes have length (L_1, L_2, L_3, L_4) = (78.6, 10.0, 43.7, 122.4) cm and the input supplies $p_{input} = 102.7$ kPa for $t_{input} = 3.4$ sec. As shown in Fig. 5c, for this set of parameters both the numerical model (solid lines) and the experimental observations (dashed lines) closely follow the target response, i.e. the four actuators reach the specified maximum bending curvatures at the desired times (markers) and then deflate (Fig. 5d and Movie S5).

Secondly, we look for a system in which $K_{i,max} = 0.6 + 0.2(i-1)$ and $T_{i,max} = 0.15 + 0.1(i-1)$ (with $i = 1, 2, 3, 4$), so that the actuators sequentially bend with progressively increasing curvature (Fig. 5e). Our optimization algorithm converges to the optimal solution after 60 iterations (see Fig. 5f) and finds that this response can be achieved for (L_1, L_2, L_3, L_4) = (3.5, 3.0, 14.8, 43.0) cm with $p_{input} = 23.3$ kPa and $t_{input} = 5.8$ sec. Remarkably, for this case we again find that both our experiments and simulations closely match the target response (Fig. 5f, 5g and Movie S6).

We emphasize that both target responses shown in Fig. 5 would require an independently controlled input line associated with each actuator in the array, if they were to be achieved without harnessing viscous effects in the fluidic network. Therefore, by carefully selecting the narrow tubes connecting the fluidic actuators as well as the input pressure and pressurization time the target response for the system can be naturally embedded in its design, allowing for a substantial simplification in system actuation. Note that even though in Fig. 5 we focus on two responses, our strategy is robust and can be used to achieve a wide variety of responses (Supplementary Materials). Finally, it is important to note that in cases where the careful selection of the narrow tubes, input pressure and pressurization time through optimization lead to system responses that do not closely approach the objective, the solution space can be further enriched by further optimizing the geometry of the fluidic actuators (Supplementary Materials). However, from a practical point of view, optimizing the geometry of the fluidic actuators is not always desirable, since it requires the fabrication of new actuators.

Multi–Objective Optimization

The results of Fig. 5 demonstrate the robustness of our approach in identifying systems capable of achieving a desired target response. However, in many cases soft robots need to be able to achieve multiple different responses and easily switch from one to another. To this end, we investigate whether varying the magnitude of input pressure P_{input} and pressurization time T_{input} is sufficient to enable a single system to achieve more than one target responses. Performing a brute–force search for the range of responses that a system optimized for a specific sequence can achieve just by varying P_{input} and T_{input}, we find that the inflation parameters have very little effect in changing the initial response for which the system was optimized (Supplementary Materials).

Therefore, to effectively identify a system capable of switching from one desired response (Target 1) to another (Target 2) just by varying the inflation parameters, we formulate a multi–objective optimization problem. The dimensionless tube parameters ξ_i (with $i = 1, 2, 3, 4$) and the inflation parameters associated to the two target responses (i.e. ($P_{input}^{(1)}$, $T_{input}^{(1)}$) and ($P_{input}^{(2)}$, $T_{input}^{(2)}$)) are obtained by minimizing

$$\mathcal{Z} = \alpha \mathcal{Z}^{(1)} + (1 - \alpha)\mathcal{Z}^{(2)} \tag{11}$$

where $\mathcal{Z}^{(1)}$, $\mathcal{Z}^{(2)}$ are the objective functions corresponding to Target 1 and Target 2 and $\alpha \in [0, 1]$ is a scalar weighing the relative importance of each objective. Focusing on a system capable of switching between the two responses defined by the anchor points shown in Figs. 6a and b, our optimization algorithm finds that both objectives are best approached for $\alpha = 0.5$ (Fig. 6c) when (L_1, L_2, L_3, L_4) = (16.5, 10.0, 48.0, 124.0) cm, $p_{input}^{(1)} = 39.6$ kPa, $t_{input}^{(1)} = 6.32$ sec, $p_{input}^{(2)} = 58.5$ kPa and $t_{input}^{(2)} = 3.33$ sec. The corresponding numerical (solid lines) and experimental (dashed lines) responses are again in excellent agreement for both system responses and come sufficiently close to both objectives (Figs. 6d and e and Movie S7). Consequently, our multi–objective optimization approach can be used to successfully design systems that can achieve different target responses just by varying the input pressure magnitude P_{input} and duration T_{input}.

Conclusions

In summary, using a combination of optimization tools and experiments we have shown that viscous flow in the tubes interconnecting fluidic actuators can be exploited to design soft robots that, albeit inflated via a single input, are capable of achieving a wide range of target responses. Throughout our study, we have found an excellent agreement between the numerical predictions and experimental findings - a clear indication of the predictive

power and robustness of our framework. Even though in this work we focused on systems in which the actuators inflate according to a target sequence, we believe that our strategy can be directly applied to design a wide range of fluid actuated soft robots capable of performing multiple different tasks using a single input. To demonstrate how actuation sequencing through viscous flow can simplify the actuation of fluidic soft robots, we design a soft robot that comprises the four bending actuators considered throughout this study (with top layer thicknesses t = 4.0, 2.9, 2.1 and 1.5 mm), connect Actuator 1 (t = 4.0 mm) to the pressure input via a tube with L_1 = 78.6 cm and R_1 = 0.38 mm and supply p_{input} = 102.7 kPa for t_{input} = 3.4 sec. If the four actuators are interconnected using tubes that do not impose significant restrictions to fluid flow (i.e. R_i = 0.79 mm for i = 2, 3, 4), only the most compliant actuator inflates and no functionality is achieved (Movie S8). In contrast, if the actuators are connected using the tube lengths that correspond to the optimal solution of Figs. 5a and b (Fig. 7a), the soft robot walks in a consistent and predictable manner covering a distance of $\simeq$ 15 cm over 10 inflation cycles (Fig. 7b and Movie S8). Finally, while in this study we only considered objectives for which a single curvature-time point was sufficient to describe the desired response of each actuator, one could differently focus on the smooth control of fluidic actuators and define an objective function in terms of multiple target points in the curvature-time space for each actuator. We expect that very few modifications would be necessary to achieve a smoother response for every actuator, since viscous flow is inherently a "smoothing" process.

References

[1] D. Trivedi, C. D. Rahn, W. M. Kier, I. D. Walker, *Applied Bionics and Biomechanics* **3**, 99 (2008).

[2] F. Ilievski, A. D. Mazzeo, R. F. Shepherd, X. Chen, G. M. Whitesides, *Angewandte Chemie International Edition* **50**, 1890 (2011).

[3] R. F. Shepherd, *et al.*, *Proceedings of the National Academy of Sciences* **108**, 20400 (2011).

[4] S. Kim, C. Laschi, B. Trimmer, *Trends in Biotechnology* **31**, 287 (2013).

[5] M. Carmel, *Soft Robotics* **1**, 5 (2014).

[6] D. Rus, M. T. Tolley, *Nature* **521**, 467 (2015).

[7] C. Laschi, B. Mazzolai, M. Cianchetti, *Science Robotics* **1** (2016).

[8] H. Zhao, K. O'Brien, S. Li, R. F. Shepherd, *Science Robotics* **1** (2016).

[9] Y. Dian, *et al.*, *Advanced Materials Technologies* **1**, 1600055 (2016).

[10] P. Polygerinos, *et al.*, *Advanced Engineering Materials* p. 1700016 (2017). 1700016.

[11] G. Krishnan, J. Bishop-Moser, C. Kim, S. Kota, *Journal of Mechanisms and Robotics* **7**, 041014 (2015).

[12] M. T. Tolley, *et al.*, *Soft Robotics* **1**, 213 (2014).

[13] A. Rafsanjani, Y. Zhang, B. Liu, S. M. Rubinstein, K. Bertoldi, *Science Robotics* **3** (2018).

[14] S. A. Morin, *et al.*, *Science* **337**, 828 (2012).

[15] P. Polygerinos, Z. Wang, K. C. Galloway, R. J. Wood, C. J. Walsh, *Robotics and Autonomous Systems* **73**, 135 (2015). Wearable Robotics.

[16] P. Paoletti, G. W. Jones, L. Mahadevan, *Journal of The Royal Society Interface* **14** (2017).

[17] J. T. B. Overvelde, T. Kloek, J. J. A. D'haen, K. Bertoldi, *Proceedings of the National Academy of Sciences* **112**, 10863 (2015).

[18] P. Rothemund, *et al.*, *Science Robotics* **3** (2018).

[19] N. Napp, B. Araki, M. T. Tolley, R. Nagpal, R. J. Wood, *2014 IEEE International Conference on Robotics and Automation (ICRA)* (2014), pp. 1440–1445.

[20] F. Connolly, C. J. Walsh, K. Bertoldi, *Proceedings of the National Academy of Sciences* **114**, 51 (2017).

[21] Y. Dian, *et al.*, *Advanced Materials* **27**, 6323 (2015).

[22] C. C. Futran, S. Ceron, B. M. Murray, R. F. Shepherd, K. H. Petersen (2018).

[23] E. Menon, *Piping calculations manual*, McGraw-Hill calculations (McGraw-Hill, 2005).

[24] N. Hansen, S. D. Müller, P. Koumoutsakos, *Evolutionary Computation* **11**, 1 (2003).

[25] A. N. Gent, *Rubber Chemistry and Technology* **69**, 59 (1996).

[26] R. W. Ogden, *Non-linear elastic deformations* (Chichester : E. Horwood, New York, 1984).

[27] P. K. Kundu, I. M. Cohen, D. R. Dowling, eds., *Fluid mechanics* (Academic Press, Boston, 2016), sixth edition edn.

[28] G. K. Batchelor, *An Introduction to Fluid Dynamics*, Cambridge Mathematical Library (Cambridge University Press, 2000).

[29] J. Pfitzner, *Anaesthesia* **31**, 273 (1976).

Acknowledgments

Funding: Research was supported by the NSF under grant number DMR-1420570. Author contributions: N.V., J.T.B.O., and K.B. designed research; N.V. performed research; N.V., J.T.B.O. and K.B. analyzed data; N.V., A.J.G. and S.S. performed experiments; A.J.G. helped design experiments; N.V. and K.B. wrote the paper.

Supplementary materials

Supplementary sections S1 to S2

Fig. S1. 3D model of the bending actuator considered in this study.

Fig. S2. A 3D render of Parts I, II and III of the mold used to cast our fluidic bending actuators.

Fig. S3. Snapshots of the 12 steps required for the fabrication of our fluidic bending actuators.

Fig. S4. Experimental pressure–volume curves for four actuators characterized by $t = 1.5$, 2.1, 2.9 and 4.0 mm.

Fig. S5. Determining the curvature of fluidic bending actuators upon inflation

Fig. S6. Finite Element simulations.

Fig. S7. Experimental setup for testing arrays of interconnected fluidic actuators.

Fig. S8. Array of interconnected fluidic bending actuators.

Fig. S9. Array of interconnected fluidic bending actuators.

Fig. S10. Minor Losses in the tubes.

Fig. S11. A simple system consisting of a single narrow tube, a single fluidic actuator and a pressure source supplying a constant pressure

Fig. S12. Optimal solutions to the inverse problem for a system comprising four bending

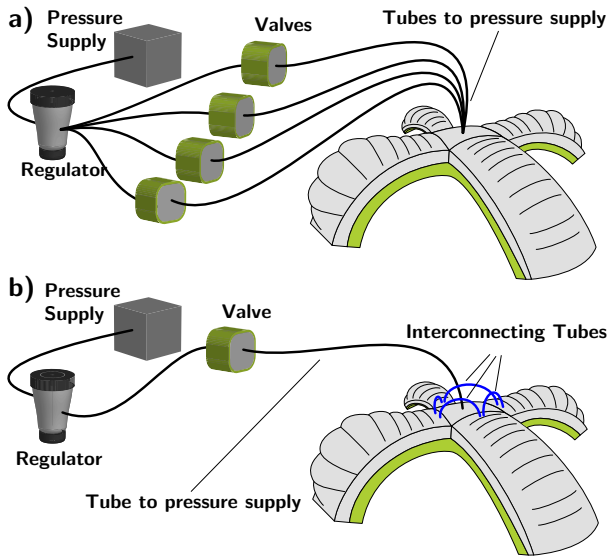

Figure 1: Simplifying the actuation of fluidic soft robots. (a) Each actuator is typically inflated and deflated independently and individually, requiring a complex actuation process. (b) In this study, we exploit viscous flow in the tubes interconnecting the constituent actuators to design soft robots capable of achieving a variety of responses when inflated with a single pressure input.

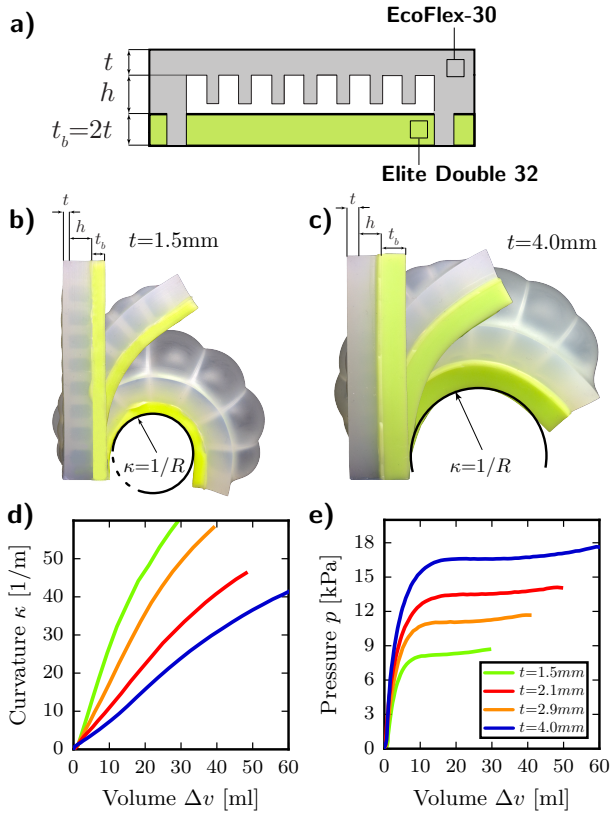

Figure 2: Fluidic bending actuators. (a) Schematic of the cross section of a fluidic bending actuator. The two different elastomers used to fabricate the sample, Ecoflex–30 (Smooth–On, Inc.) and Elite Double 32 (Zhermack) are shown in gray and green, respectively. (b)-(c) Snapshots of fluidic bending actuators characterized by (b) $t = 1.5$ mm and (c) $t = 4.0$ mm at different actuation pressures. (d) Experimental curvature–volume curves for four actuators characterized by $t = 1.5$, 2.1, 2.9 and 4.0 mm. (e) Experimental pressure–volume curves for four actuators characterized by $t = 1.5$, 2.1, 2.9 and 4.0 mm.

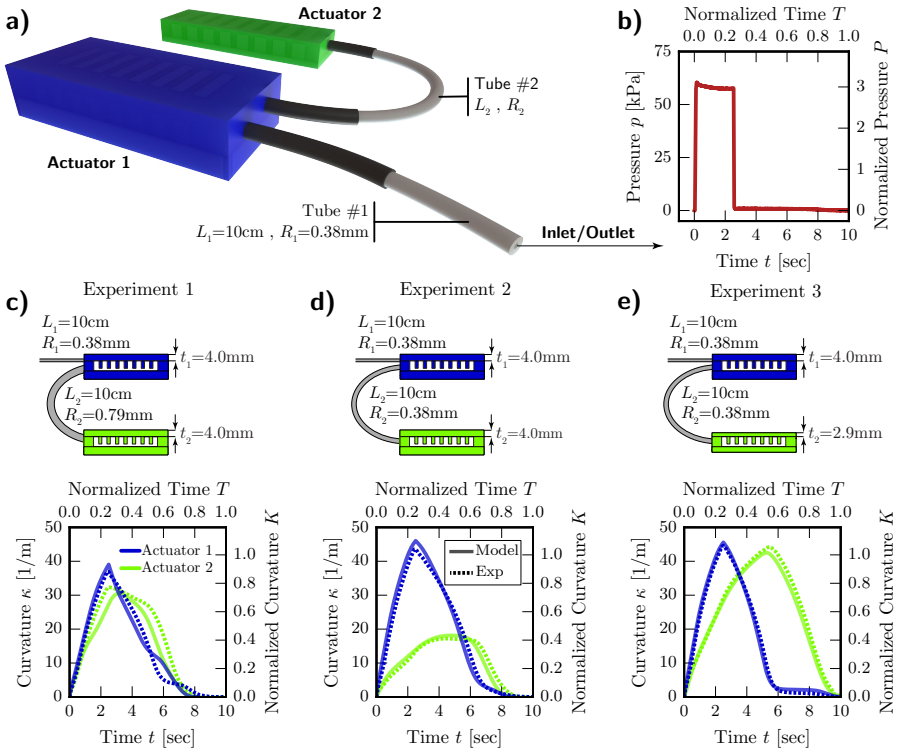

Figure 3: Harnessing viscous flow in the tubes. (a) Schematic of the system considered in all three experiments. Tube 1 connects the input pressure to the first actuator whereas Tube 2 connects the two actuators. Tube 1 has length $L_1 = 10$ cm and radius $R_1 = 0.38$ mm in all three experiments. (b) The rectangular pressure pulse used in all three experiments supplies $p_{input} = 60$ kPa for $t_{input} = 2.5$ sec. For $t > t_{input}$, $p_{input} = 0$ kPa and Tube 1 acts as an outlet for the system to reset/deflate. (c)-(e) Schematics of the configuration tested in the three different experiments (top) and corresponding curvature responses for the two actuators (bottom).

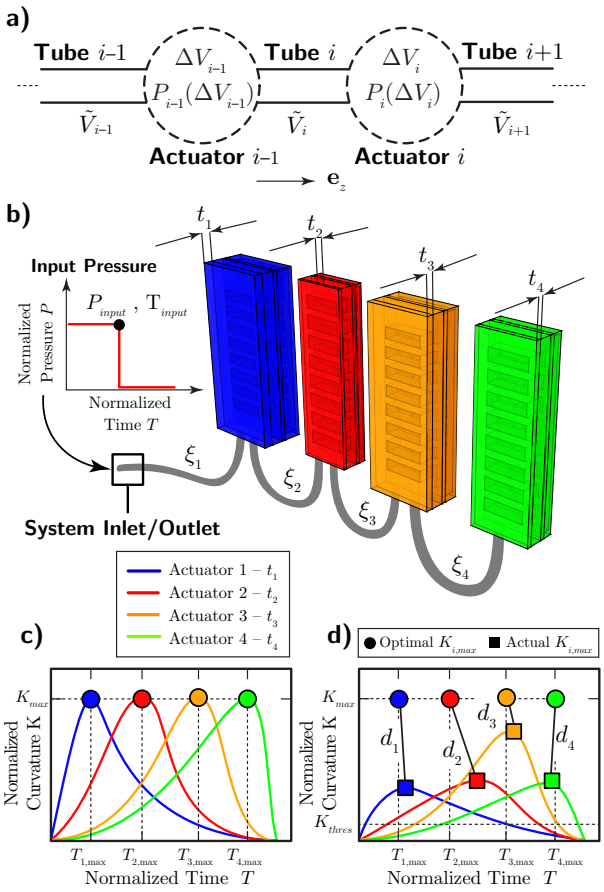

Figure 4: Forward and inverse modeling. (a) Schematic of the system. The $[i]$–th tube is connected to the $[i-1]$–th and $[i]$–th actuators. (b) Schematic of the configuration considered in the inverse problem, consisting of 4 fluidic bending actuators with thickness $t = 4.0$, 2.9, 2.1 and 1.5 mm connected via narrow tubes and inflated by a rectangular pressure pulse. (c) The target response requires the $[i]$–th actuator in the array to attain a maximum bending curvature of $K_{i,\,max}$ at a predefined time $T_{i,max}$ and then to completely deflate. (d) Parameters introduced to construct the objective function.

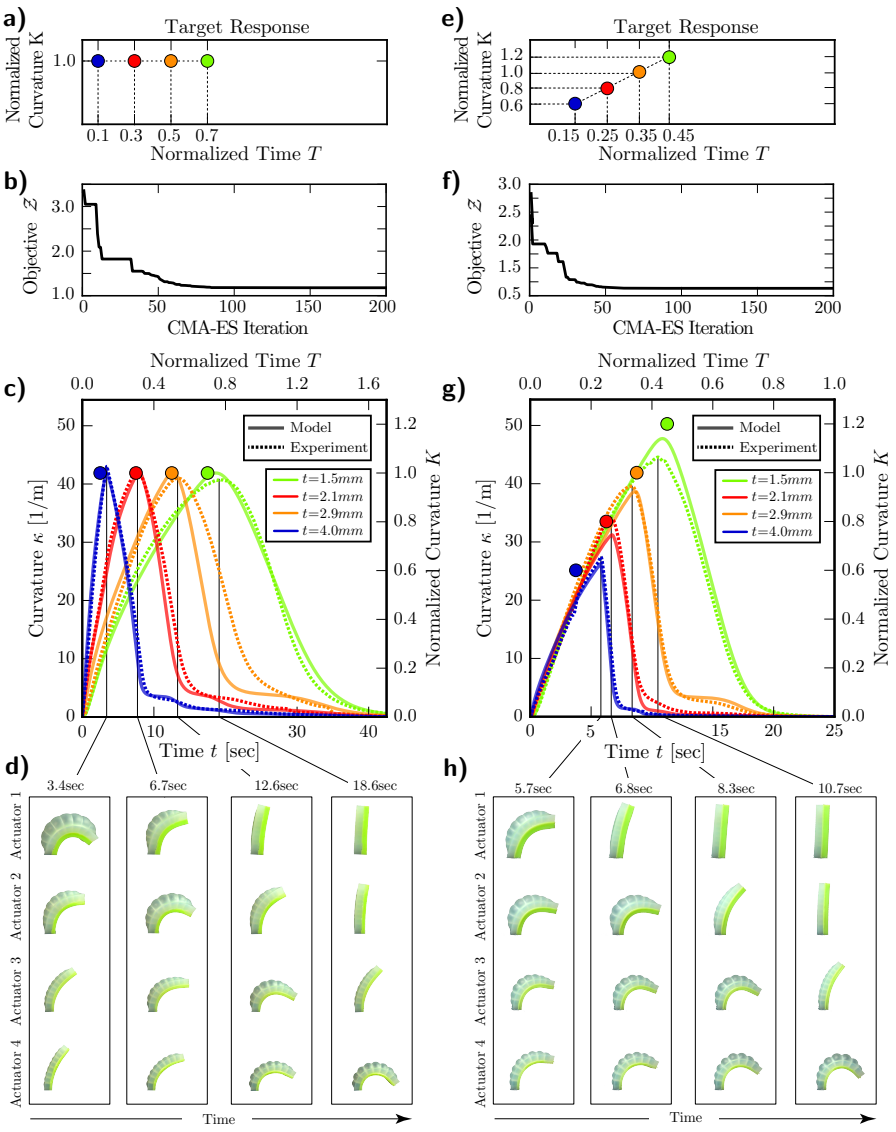

Figure 5: Solution of the inverse problem. (a) The first target response requires all actuators in the system to achieve the same maximum bending curvature $K_{i,max} = 1.0$ but at different times $T_{i,max} = 0.1 + 0.2(i-1)$ (with $i = 1$, 2, 3 and 4) (b) Evolution of the objective function during CMA-ES iterations. (c) Curvature response for the optimal system, as determined from the numerical model (solid lines) and experiments (dashed lines). (d) Snapshots of the four actuators at $T = 0.13, 0.27, 0.5, 0.74$, corresponding to the times at which each actuator achieves its maximum curvature during the experiment. (e) The second target response requires all actuators in the system to achieve the maximum bending curvature $K_{i,max} = 0.6 + 0.2(i-1)$ at $T_{i,max} = 0.15 + 0.1(i-1)$ (with $i = 1$, 2, 3 and 4). (f) Evolution of the objective function during CMA-ES iterations. (g) Curvature response for the optimal system, as determined from the numerical model (solid lines) and experiments (dashed lines). (h) Snapshots of the four actuators at $T = 0.23, 0.27, 0.33, 0.43$, corresponding to the times at which each actuator achieves its maximum curvature during the experiment.

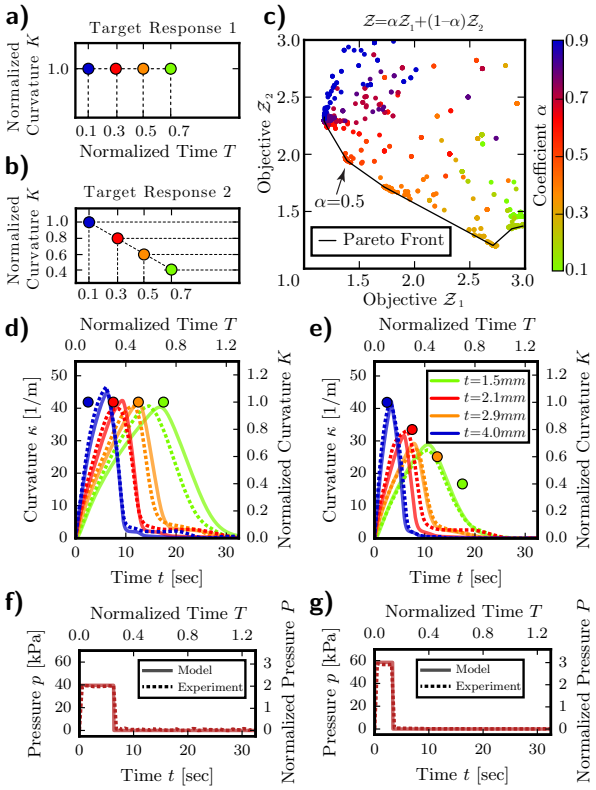

Figure 6: Multi–objective optimization. (a) - (b) The curvature anchor points defining Target 1 (a) and Target 2 (b), respectively. (c) Pareto front. The black line connects members of the pareto set. The color of the markers corresponds to value of α used in the optimization. The overall optimal solution that most closely approaches both objectives is found for $\alpha = 0.5$. (d)-(e) Numerical (solid lines) and experimental (dashed lines) curvature responses for the optimal solution of the multi–objective inverse problem for Target 1 (d) and Target 2 (e), respectively. (f)-(g) Input pressures required to achieve Target 1 (f) and Target 2 (g), as determined from the solution of the multi-objective inverse problem (solid lines) and as provided in experiments (dashed lines).

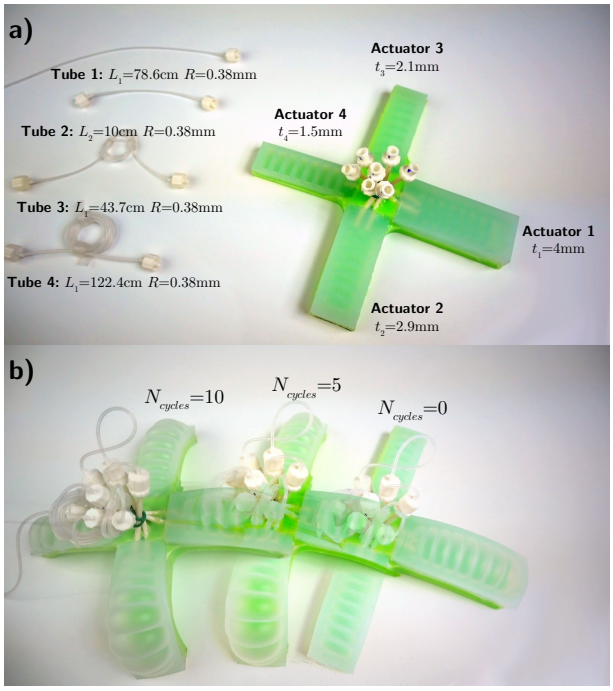

Figure 7: Actuating a four legged fluidic soft robot using a single pressure input. (a) The four actuators considered throughout this study are interconnected using narrow tubes with length (L_1, L_2, L_3, L_4) =(78.6, 10.0, 43.7, 122.4) cm and radius R = 0.38 mm. Tube 1 is connected to a pressure input supplying the robot with p_{input} = 102.7 kPa for t_{input} = 3.4 sec every 40 sec. (b) Snapshots of the position of the soft robot after 5 and 10 inflation cycles, demonstrating its ability to walk in a predictable and consistent manner (Movie S8).